

# A Progressive Image Restoration Network for High-order Degradation Imaging in Remote Sensing

Yujie Feng, Yin Yang, Xiaohong Fan, Zhengpeng Zhang, Lijing Bu and Jianping Zhang

**Abstract**—Recently, deep learning methods have gained remarkable achievements in the field of image restoration for remote sensing (RS). However, most existing RS image restoration methods focus mainly on conventional first-order degradation models, which may not effectively capture the imaging mechanisms of remote sensing images. Furthermore, many RS image restoration approaches that use deep learning are often criticized for their lacks of architecture transparency and model interpretability. To address these problems, we propose a novel progressive restoration network for high-order degradation imaging (HDI-PRNet), to progressively restore different image degradation. HDI-PRNet is developed based on the theoretical framework of degradation imaging, offering the benefit of mathematical interpretability within the unfolding network. The framework is composed of three main components: a module for image denoising that relies on proximal mapping prior learning, a module for image deblurring that integrates Neumann series expansion with dual-domain degradation learning, and a module for super-resolution. Extensive experiments demonstrate that our method achieves superior performance on both synthetic and real remote sensing images.

**Index Terms**—High-order degradation model, image restoration, remote sensing image, deep unfolding network.

## I. INTRODUCTION

REMOTE sensing images contained abundant spatial texture details and scene semantic information, which have been widely applied in tasks such as scene segmentation [1]. However, due to the complex environment of remote sensing imaging and the inherent limitations of sensor hardware, the observed remote sensing images inevitably degrade. The low quality of remote sensing images limits their practical application in high-level remote sensing tasks directly. To address this problem efficiently with minimal cost, employing image restoration techniques is optimal, as it avoids the need

for upgrading equipment. These techniques reconstruct a high-resolution (HR) image, enriched with detailed high-frequency textures, from a low-resolution (LR) image. As a result, image restoration has become increasingly popular in the fields of remote sensing and computer vision.

The classical first-order image degradation model can be expressed mathematically as follows

$$g = (h * u)_{\downarrow_s} + n, \quad (1)$$

where  $g$  is the observational LR image,  $u$  is the HR image with sharp details,  $h$  is the blur kernel,  $n$  is the additive white gaussian noise (AWGN), and  $*$  denotes the 2-D convolution operator,  $\downarrow_s$  denotes the downsampling operator with scale factor  $s$ .

The restoration of degradation images in remote sensing is a challenging task, as it involves restoring the sharp HR image  $u$  from the deteriorated LR image  $g$ . This problem (1) is considered ill-posed because there are multiple HR solutions that can map to the same LR image, resulting in a non-unique solution. Various methods [2]–[4] for image restoration have been investigated. Although many algorithms ignore blur and noise degradation in the forward model (1) and rely solely on the ideal bicubic operator to simulate the super-resolution degradation model, these approaches do not align with the actual physical imaging mechanism of remote sensing, rendering these algorithms impractical in real-world remote sensing applications [5], [6].

Recently, numerous deep learning-based methods have been proposed for image restoration [7]–[14] and have demonstrated strong performance across various datasets and evaluation metrics. These methods aimed to integrate advanced deep learning modules and techniques such as channel attention mechanisms [10], spatial attention mechanisms [11], transformer mechanisms [12], and generative adversarial networks (GANs) [15]. The primary aim of these methods is to learn the mapping between LR and HR images. However, several challenges remain. 1) Most super-resolution algorithms use the first-order degradation model, which is inadequate for real images as these are often affected by high-order complex degradations; 2) the end-to-end black-box nature of deep learning-based algorithms makes it challenging to distinguish how the network architecture influences its prediction, emphasizing the need for enhanced transparency and interpretability in these frameworks; 3) many deep learning techniques focus on designing sophisticated network modules and depend on expanding them deeper and wider to enhance performance, this results in increased computational needs and challenges related to the smart design of network architectures.

This work was supported by the National Key Research and Development Program of China (2020YFA0713503), the science and technology innovation Program of Hunan Province (2024RC9008), the Project of Scientific Research Fund of the Hunan Provincial Science and Technology Department (2022RC3022, 2023GK2029, 2024ZL5017, 2024JJ1008), and Program for Science and Technology Innovative Research Team in Higher Educational Institutions of Hunan Province of China. Corresponding authors: J. Zhang (e-mail: jpzhang@xtu.edu.cn) and Y. Yang (e-mail: yangyinxu@xtu.edu.cn).

Y. Feng is with the School of Mathematics and Computational Science, Xiangtan University, Hunan Key Laboratory for Computation and Simulation in Science and Engineering, Key Laboratory for Intelligent Computing and Information Processing of the Ministry of Education, Xiangtan 411105, China.

Y. Yang and J. Zhang are with the School of Mathematics and Computational Science, Xiangtan University, National Center for Applied Mathematics in Hunan, Hunan International Scientific and Technological Innovation Cooperation Base of Computational Science, Xiangtan 411105, China.

X. Fan is with the College of Mathematical Medicine, Zhejiang Normal University, Jinhua 321004, China.

Z. Zhang and L. Bu is with the School of Automation and Electronic Information, Xiangtan University, Xiangtan 411105, China.

To address these problems, we introduce a high-order degradation model to describe the combined effects of various complex degradations in remote sensing imaging, including atmospheric transmission degradation, sensor imaging system degradation, satellite platform flutter degradation, etc. Based on the high-order degradation imaging, we propose a new high-order progressive restoration network, called HDI-PRNet, which aims to recover multiple layers of degradation. Specifically, each stage of this model is composed of three components: a module for image denoising that relies on proximal mapping prior learning, a module for image deblurring that integrates Neumann series expansion with dual-domain degradation learning, and a module for super-resolution. The main contributions in this paper can be summarized as follows.

- We introduce a novel high-order progressive remote sensing restoration network, termed HDI-PRNet, constructed around a high-order backward degradation model. Our framework adeptly manages complex degradation mechanisms, notably enhancing restoration performance, particularly in real remote sensing applications. The structures aligning backward degradation tasks with respective modules render HDI-PRNet more transparent and interpretable.
- A denoising module is developed using proximal mapping operator learning. By leveraging the multi-scale encoder-decoder learning and attention mechanisms, it emphasizes crucial denoising prior details required at each stage while preserving fine detail information.
- We design a deblurring module that leverages the Neumann series expansion in combination with a dual-domain backward degradation learning block. This approach efficiently acquires prior knowledge of blur degradation operators in both spatial and frequency domains, leading to the integration of dual-domain representations.
- Experimental results confirm that the HDI-PRNet framework can obtain high-quality restored images on various randomly degraded synthetic low-resolution images and real remote sensing images.

This paper is organized as follows. Section II covers related work in image restoration. Our proposed HDI-PRNet framework is detailed in Section III. We analyze our experimental results and ablation experiments in Section IV. Finally, Section V presents the conclusions.

## II. RELATED WORK

In this section, we briefly review the related works on natural image restoration algorithms, remote sensing image restoration algorithms, and multiple degradation models.

### A. Image restoration for natural images

Recently, with the rapid development of neural network technology, deep learning methods have achieved excellent performance in the field of computer vision. Dong et al. [16] proposed SRCNN, which first applied a three-layer convolutional neural network for image super-resolution (SR). Zhang et al. [17], [18] proposed the residual dense block (RDB), which fully utilizes all of the layers in it through

local dense connections, and proposed the residual dense network (RDN). Zhang et al. [10] proposed the structure of residuals in residuals (RIR) to form very deep networks, and also proposed the residual channel attention network (RCAN) for image SR. Zamir et al. [19] introduced Restormer, a transformer model that performs well in a variety of image restoration tasks. Meanwhile, Fan et al. [4] developed an incremental learning framework, called Nest-DGIL, using Nesterov's method to reconstruct images from compressed sensing data. Dai et al. [20] proposed a high-order attention network for single image SR (SAN). Liang et al. [12] proposed an image restoration model based on the Swin Transformer (SwinIR), and achieved good performance in image SR task, image denoising and JPEG artifact removal tasks. Mei et al. [21] proposed a novel non-local sparse attention (NLSA) with dynamic sparse attention pattern for image SR. Cui et al. [8] introduced FSNNet, an image restoration network focusing on frequency information selection. Chen et al. [9] introduced a nonlinear activation-free network (NAFNet), which offers a simplified and efficient baseline for recovery models by replacing the activation function with multiplication. Chen et al. [22] proposed the dual aggregation transformer (DAT), which aggregates spatial-channel features in the interblock and intra-block, achieving powerful feature representation capabilities and achieving fascinating performance on SR task. While these algorithms have demonstrated fascinating results in natural image restoration tasks, they often prioritize the development of complex high-performance learning modules and neglecting the interpretability of the network structure.

### B. Image restoration for remote sensing images

Nowadays, with the increasing application of remote sensing images in various fields, the remote sensing image restoration algorithms have attracted increasing attention. They can improve the quality of remote sensing images, restoring more distinct details compared to the original low-quality images, without equipment upgrades.

With the development of deep learning and the success of natural image processing algorithms, lots of remote sensing image restoration algorithms have been proposed. Lei et al. [23] designed a combined local-global network (LGCNet), which learns multilevel feature representations of images through different convolutional layers and global-local features of ground objects and environmental priors, to reconstruct high-quality remote sensing images. Zhang et al. [24] proposed a kind of novel mixed high-order attention network (MHAN) to fully exploit hierarchical features for detail restoration. Xu et al. [25] designed a global-local fusion-based cloud removal algorithm (GLF-CR) that combines synthetic aperture radar and optical image feature information for remote sensing image cloud removal. Xiao et al. [26] designed a top-k token selective transformer (TTST) for remote sensing image super-resolution to flexibly filter information in self-attention. Wang et al. [27] proposed a novel U-shaped network based on hybrid attention (HAUNet), which is designed based on a multiscale structure and a hybrid convolutional attention mechanism to enhance the representation of global features.

Lei et al. [28] proposed the transformer-based enhancement network (TransENet), which utilizes the transformer block to extract the high/low-dimensional features to enhance the representation of high dimensions features. TransENet performs well on the synthetic UCMcred and AID dataset.

However, most of these image restoration algorithms use simple bicubic downsampling to simulate remote sensing image degradation, which is inconsistent with real remote sensing degradation. This is one of the reasons why the algorithms perform poorly on real remote sensing images. In order to solve this problem, we design a network based on a high-order degradation model that is closer to real degradation.

### C. Multiple degradation models

The first-order degradation model (1) is widely used in image restoration algorithms and has achieved good performance. Most of these algorithms simplify degradation into a simple bicubic downsampling process. However, real-world imaging degradation is a complex, multi-faceted process, and simple bicubic downsampling limits the robustness of the algorithm and does not accurately simulate real-world image degradation. Wang et al. [29] proposed a high-order degradation model that simulates complex real-world degradation by combining multiple degradations (including blur, noise, downsampling, etc.), and achieved excellent real-world super-resolution results. Zhang et al. [30] proposed a complex degradation model which consists of multiple random shuffled degradations. Potlapalli et al. [31] designed a prompt learning restoration network (PromptIR) for different types of degradation, providing a versatile and efficient plug-in module with few lightweight prompts that can be used to restore images of various types and degradation levels. Kong et al. [32] proposed a sequential learning strategy and a prompt learning strategy for all-in-one image restoration. These two strategies have good effects on the CNN and Transformer backbones, and they can promote each other to learn effective image representations. In comparison, our work is focused on developing an unfolding network for real remote sensing image restoration that is conceptually simple but more interpretable.

## III. METHODOLOGY

This section first briefly introduces the high-order degradation model, followed by a detailed explanation of the proposed progressive restoration architecture designed to solve high-order degradation imaging. We also introduce a multi-supervising loss function to train the proposed architecture.

### A. High-order Degradation Model

An image degradation model is formulated to simulate the mechanisms that lead to a decrease in image quality [33], [34]. The classical first-order image degradation (1) is rewritten as

$$\mathbf{g} = \mathcal{D}(\mathbf{u}) = (\mathbf{h} * \mathbf{u})_{\downarrow_s} + \mathbf{n},$$

where  $\mathcal{D}$  denotes the degradation operator, it includes factors such as the blur, downsampling, and noise degradation. However, the first-order model described above remains inadequate

for addressing certain complicated real-world degradation, particularly unknown noises and complex artifacts. The authors in [29] improve the first-order degradation model by extending it to a more flexible higher-order degradation to better represent real-world degradations, as defined by

$$\mathbf{g} = \mathcal{D}_k(\cdots \mathcal{D}_2(\mathcal{D}_1(\mathbf{u}))), \quad (2)$$

where  $\mathcal{D}_\ell$  denotes the  $\ell$ -th imaging sub-system or degradation sensor ( $1 \leq \ell \leq k$ ).

In this work, we decompose the  $k$ -order degradation framework into a series of  $k$  sequential first-order models, described as follows

$$\begin{aligned} \mathbf{g}_1 &= \mathcal{D}_1(\mathbf{u}) = \mathcal{N}_1(\mathcal{S}_1(\mathcal{B}_1(\mathbf{u}))) \\ \mathbf{g}_2 &= \mathcal{D}_2(\mathbf{g}_1) = \mathcal{N}_2(\mathcal{S}_2(\mathcal{B}_2(\mathbf{g}_1))) \\ &\dots \\ \mathbf{g} := \mathbf{g}_k &= \mathcal{D}_k(\mathbf{g}_{k-1}) = \mathcal{N}_k(\mathcal{S}_k(\mathcal{B}_k(\mathbf{g}_{k-1}))), \end{aligned} \quad (3)$$

where the functions  $\mathcal{B}_k(\cdot)$ ,  $\mathcal{S}_k(\cdot)$ ,  $\mathcal{N}_k(\cdot)$  represent the blur, downsampling, and noise degradation operators, respectively. The formula (3) outlines a hierarchical degradation model that provides a more precise representation of the real remote sensing imaging system.

### B. Algorithm

The restoration algorithm based on Eq. (3) can be divided into  $k$  stages to be solved progressively, where  $k$  stages correspond to the high-order degradation mechanism. We assume  $\mathbf{g}_0 = \mathbf{u}$ ,  $\mathbf{g}_\ell = \mathcal{D}_\ell(\mathbf{g}_{\ell-1})$  ( $1 \leq \ell \leq k$ ) and  $\mathbf{g}_k = \mathbf{g}$ . The energy minimization model at  $\ell$ -stage can be written as

$$\mathbf{g}_{\ell-1} = \arg \min_{\mathbf{g}} \|\mathbf{g}_\ell - \mathcal{S}_\ell(\mathcal{B}_\ell(\mathbf{g}))\|_2^2 + \lambda_\ell f_\ell(\mathbf{g}), \quad (4)$$

where the regularization  $f_\ell(\cdot)$  can be used to constrain the geometric prior of a given image in denoising subproblem.

There have been several excellent explorations in solving (4). One of main categories involves step-by-step degradation representations and typically consists of three components: prior denoising or local filtering, super-resolution or interpolation, and blind degradation prediction. The above three components are performed either separately (iteratively) or jointly. Therefore, the above energy minimization model (4) can be divided into three sub-problems, as follows

$$\mathbf{g}_\ell^{dn} = \arg \min_{\mathbf{g}} \|\mathbf{g} - \mathbf{g}_\ell\|_2^2 + \lambda_\ell f_\ell(\mathbf{g}), \quad (5)$$

$$\mathbf{g}_\ell^{sr} \in \{\mathbf{g} | \mathcal{S}_\ell(\mathbf{g}) = \mathbf{g}_\ell^{dn}\}, \quad (6)$$

$$\mathbf{g}_{\ell-1} := \mathbf{g}_\ell^{db} \in \{\mathbf{g} | \mathcal{B}_\ell(\mathbf{g}) = \mathbf{g}_\ell^{sr}\}. \quad (7)$$

The classical solution methods of the above subproblems depend on the types and levels of degradation, and the forward simulation typically involves straightforward synthetic degradations. Furthermore, any imprecise estimations of degradation in real images will unavoidably lead to artifacts. Therefore, the following literature will focus on developing a progressive unfolding restoration network for real remote sensing imaging.

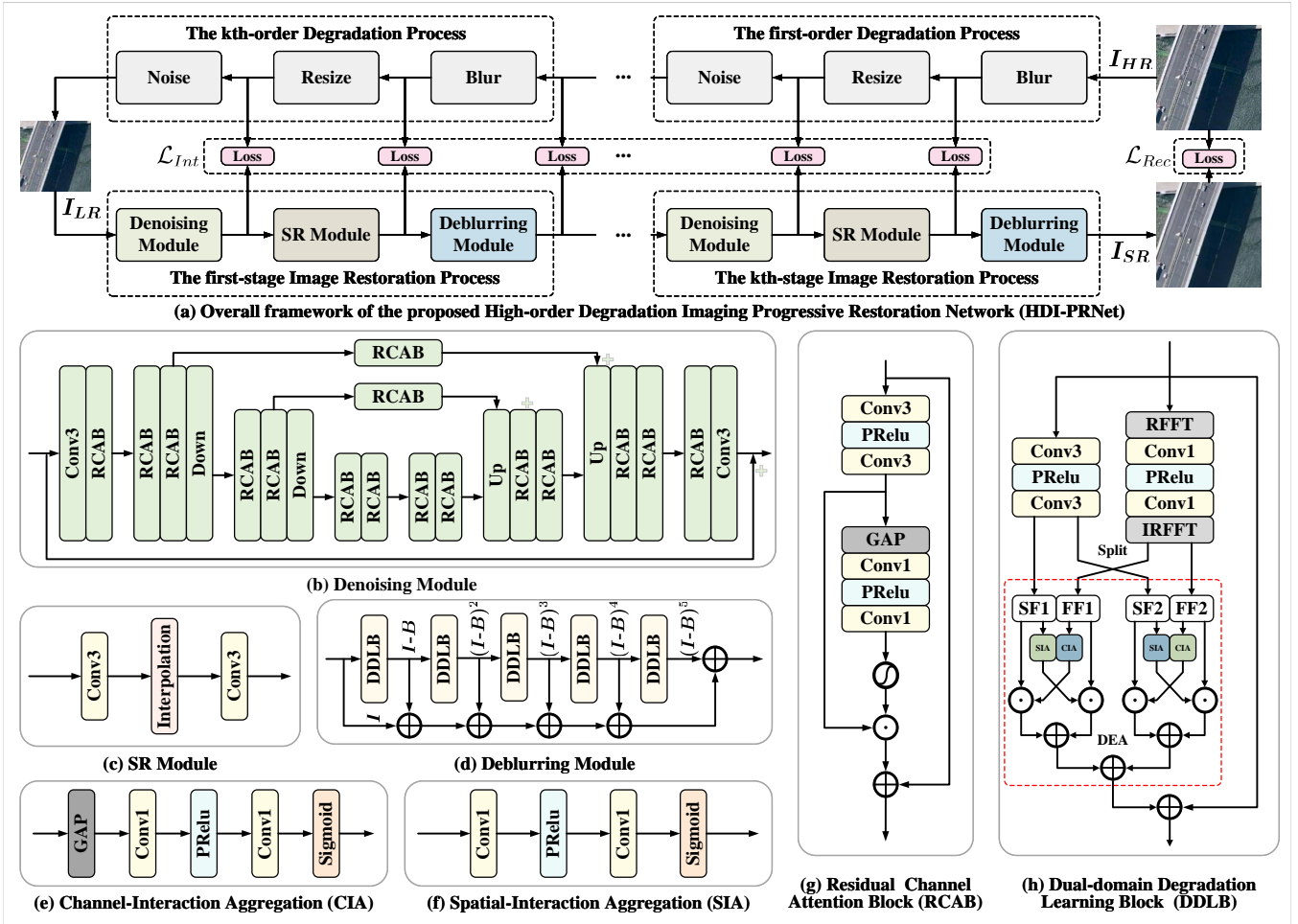


Fig. 1. The overall framework of the proposed HDI-PRNet solving the high-order degradation model.

### C. Proposed Framework

1) *Overall Architecture*: Deep neural networks with their powerful non-linear representation capabilities have become increasingly popular in addressing reconstruction challenges associated with degraded data. Building upon the progressive operator splitting theory described above, we construct a deep unfolding network for the degradation reconstruction. The overall framework we propose is shown in Fig. 1(a).

The input variable  $g_\ell$  at  $\ell$ -stage first undergoes a deep prior unfolding denoising sub-network to obtain the clean approximation  $g_\ell^{dn}$ . In addition, the super-resolution distillation SR module is proposed to exploit the structural characteristics among different features by interpolating multiscale representations, thereby improving the resolution of an image  $g_\ell^{dn}$  and improving image quality. This super-resolution estimation  $g_\ell^{sr}$  is then refined through a deep blind-deblurring sub-network, where each block corresponds to one Neumann expansion term of the blind-deblurring sub-problem. The initial reconstruction  $g_\ell^{sr}$  is processed through multiple blocks of the sub-network to achieve the final deblurring reconstruction. Specifically, our innovative network design is carried out hierarchically. The framework consists of  $k$  stages corresponding to the  $k$ -order degradation model, and each stage consists of three modules corresponding to three sub-problems (5)-(7).

To better leverage the prior information, we employ one proximal mapping subnetwork to independently solve (5), represented as the denoising module. For the subproblem of blind deblurring, we improve the feature representation capability of the network by learning truncated Neumann series to replace the direct inverse operator  $\mathcal{B}^{-1}$ . This structure ensures the robustness of the framework in handling multiple or different types of degraded image. Each degradation sub-system will solve the inverse problem progressively. Additionally, to reduce information loss between network stages, we add intermediate losses to ensure that the submodule learns the corresponding subproblem, to improve the spatio-temporal feature representation of the framework, and also to ensure the interpretability of the algorithm. The specific design of each sub-network will be introduced in the following subsections.

2) *Image denoising proximal mapping module*: The sub-problem (5) is a classical denoising optimization, which is highly effective in removing various types of noise. The solution of the optimization (5) with the general regularization term  $f_\ell$  can be given by the proximal operator as

$$g_\ell^{dn} = \mathbf{prox}_{\lambda_\ell, f_\ell}(g_\ell). \quad (8)$$

Since  $f_\ell(\cdot)$  is the geometric prior term of the solution image  $g$ , hence one of the key advantages of the sub-problem (5)

is its ability to preserve important image details. However, the regularization parameter  $\lambda_\ell$  in (5) controls the trade-off between the fidelity to the observed data and the smoothness of the image. If  $\lambda_\ell$  is larger, the denoised image is imposed stronger smoothing, leading to a potentially smoother but a loss of fine-grained details like edges, textures, and small structures. If  $\lambda_\ell$  is smaller, then the denoising effect may be weaker, resulting in an image closer to the original but potentially with more noise.

The proximal mapping module can analyze the local neighborhood of each pixel and fuse features to reduce the noise component while preserving the details of the image [35]. The optimization problem (5) provides a theoretical guarantee for the performance and convergence of the proximal mapping module. In other words, it typically operates by solving a proximal operator problem that seeks to minimize the denoising problem (5). Compared to some complex iterative denoising methods that require a large number of calculations for each pixel and multiple iterations over the entire image, the proximal mapping module can achieve good denoising results with fewer computational resources [4], [36]. This makes it suitable for real-time or near-real-time applications such as video denoising or high-throughput image processing in industrial inspection.

To obtain a more accurate prior denoising expression of (8), we design an image denoising unfolding module to learn the proximal mapping, as shown in Fig. 1(b). The proximal mapping  $\text{prox}_{\lambda_\ell, f_\ell}$  is designed as a coarse to fine architecture, uses an encoder and a decoder to learn the generalized multiscale prior  $\lambda_\ell f_\ell(\mathbf{g})$ , and then obtains the solution of (8). Firstly, the denoising module adopts a convolutional design to extract shallow prior features. Secondly, it involves three scales, and we use Residual Channel Attention Blocks (RCAB) to extract and fuse multi-scale prior features at three scales (see Fig.1(b) and (g)). The skip connections between downsampling and upsampling at each scale are also processed using RCAB, and the channel number of the three scales is set to 120, 140, and 160 at resolutions 1, 1/2, 1/4, respectively. Then, we introduce a skip connection before and after the encoder decoder to ensure the stability of proximal mapping learning. Finally, in terms of sampling operators, we use bilinear sampling to perform down-sampling and up-sampling operations.

3) *Image super-resolution module*: Image super-resolution is a method employed to improve the resolution of an image, resulting in a clearer and more detailed appearance. This enhancement is typically accomplished using algorithms and models that estimate high-resolution predictions from low-resolution inputs [37].

The CNN image super-resolution leverages deep learning techniques to enhance the resolution of images. It typically involves training a CNN model on low-resolution and high-resolution image pairs, where the network learns to reconstruct high-resolution images from their low-resolution counterparts. The proposed framework employs an SR module with convolution and pixelshuffle to solve the problem at  $\ell$ -stage as

$$\mathbf{g}_\ell^{sr} \in \{\mathbf{g} | \mathcal{S}_\ell(\mathbf{g}) = \mathbf{g}_\ell^{dn}\}, \quad 1 \leq \ell \leq k.$$

Since the proposed framework is a  $k$ -stage cascaded architecture that processes sub-problems progressively, the first-stage SR module resizes the image from the LR space to the middle resolution space, and then the final stage resizes it to the HR space. In this case, we need to perform SR tasks with a different upsampling ratio ( $\uparrow_s$ ) in the  $k$  stages. To achieve efficiently fractional super-resolution without introducing new degradation, we simply use convolution and bilinear interpolation to perform upsampling operations to solve (6), as shown in Fig. 1(c). This module can ensure that the image will not have problems such as checkerboard artifacts caused by transposed convolution. However, such an SR module can efficiently adjust the spatial resolution. Although bilinear interpolation is considered to have defects in sharpening edge details, the deblurring problem can be handled by the subsequent deblurring module.

4) *Image deblurring module*: Let the blurring operator  $\mathcal{B}_\ell$  be a bounded linear operator that satisfies  $\rho(\mathcal{I} - \mathcal{B}_\ell) < 1$  on a Banach space  $\mathcal{X}$ . The Neumann expansion series of  $\mathcal{B}_\ell^{-1}$  is given by the following infinite series

$$\mathcal{B}_\ell^{-1} = (\mathcal{I} - (\mathcal{I} - \mathcal{B}_\ell))^{-1} = \sum_{i=0}^{+\infty} (\mathcal{I} - \mathcal{B}_\ell)^i, \quad (9)$$

where  $\mathcal{I}$  is an identity operator,  $(\mathcal{I} - \mathcal{B}_\ell)^0 = \mathcal{I}$  (the identity operator) and  $(\mathcal{I} - \mathcal{B}_\ell)^i = (\mathcal{I} - \mathcal{B}_\ell) \circ \dots \circ (\mathcal{I} - \mathcal{B}_\ell)$  ( $i$  times composition of  $(\mathcal{I} - \mathcal{B}_\ell)$  with itself for  $i \geq 1$ ). To facilitate calculations, we use a  $m$ -term truncated Neumann series expansion to approximate  $\mathcal{B}_\ell^{-1}$  as follows

$$\mathbf{g}_\ell^{db} = \mathcal{B}_\ell^{-1}(\mathbf{g}_\ell^{sr}) \approx \sum_{i=0}^m (\mathcal{I} - \mathcal{B}_\ell)^i(\mathbf{g}_\ell^{sr}). \quad (10)$$

Even if the condition  $\rho(\mathcal{I} - \mathcal{B}_\ell) < 1$  is not met, the truncated Neumann series (10) can still approximate the inverse operator  $\mathcal{B}_\ell^{-1}$ , providing a form of implicit regularization [38].

To obtain accurately blur degradation, we use the Dual Domain Degradation Learning Block (DDLDB) designed based on the ResFFT-ReLU Block [39] as follows

$$\mathcal{I} - \mathcal{B}_\ell = \mathcal{I} + \mathbf{DEA}(\mathcal{B}_\ell^{Spatial}, \mathcal{B}_\ell^{Frequency}) \quad (11)$$

to learn (10), as shown in Fig. 1(d) and (h). Here, we split the blur operator  $\mathcal{B}_\ell$  into a multi-scale dual-domain feature representation. Therefore, DDLDB includes the spatial transformation branch  $\mathcal{B}_\ell^{Spatial}$ , the frequency transformation branch  $\mathcal{B}_\ell^{Frequency}$ , the dual-domain expression aggregation (DEA) and the identity transformation  $\mathcal{I}$ .

In the spatial domain branch, the **Conv-PReLU-Conv** configuration is used to learn and simulate the degradation process  $\mathcal{B}_\ell^{Spatial}$ . This structure is widely adopted in CNN architectures and has been validated to effectively capture local spatial features. Regarding the branch in the frequency domain, the image is transformed into a complex tensor  $\mathbf{z} = \mathbf{m}e^{j\beta}$  by a Fourier transform, which is divided into two components: amplitude  $\mathbf{m}$  and phase  $e^{j\beta}$ . The amplitude encodes the image's color information, whereas the phase represents the texture's positional information. Similarly to the spatial domain strategy, the **Conv-PReLU-Conv** block is used

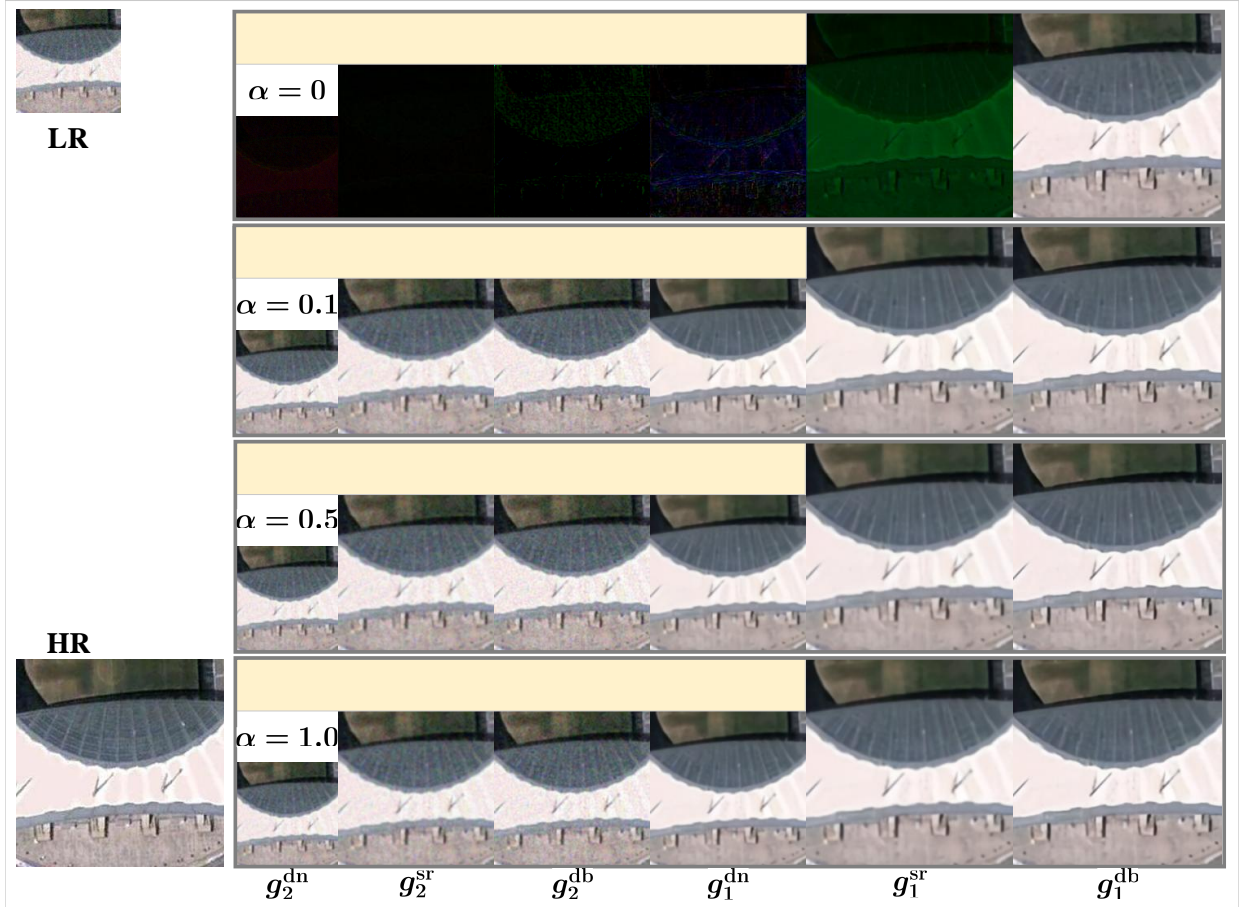


Fig. 2. Visualization comparison for different intermediate loss weight  $\alpha$ .

to model and simulate the degradation mechanism  $\mathcal{B}_\ell^{Frequency}$ . The PRelu function helps in phase selection as it satisfies  $\mathbf{PRelu}(m e^{j\beta}) = m \mathbf{PRelu}(e^{j\beta})$ . The first convolution step provides greater flexibility in phase selection, while the last convolution consolidates the selected phases to accurately express the blur operator  $\mathcal{B}_\ell^{Frequency}$ .

The representations of degradation,  $\mathcal{B}_\ell^{Spatial}$  in the spatial domain and  $\mathcal{B}_\ell^{Frequency}$  in the frequency domain, are not adequately integrated when combined solely with an addition operator. To enhance the interaction and blending of spatial and frequency domain representations, we developed the dual-domain expression aggregation (DEA), which incorporates a channel-interaction aggregation (CIA) module and a spatial-interaction aggregation (SIA) module, positioned between the spatial and frequency domain branches, illustrated in Fig. 1 (e)-(f). The application of CIA and SIA enables the adaptive synchronization of dual domain degraded features, which mutually improve their insights, refine the representation of the features and promote the integration of the degraded information.

#### D. Loss Function

The HDI-PRNet is composed of  $k$  stages, with each stage containing three sub-modules. To optimize the parameters of

these modules, we minimize the total loss, represented as

$$\mathcal{L}_{Total} = \mathcal{L}_{Rec} + \alpha \mathcal{L}_{Int}, \quad (12)$$

which consists of two components: the image reconstruction loss  $\mathcal{L}_{Rec}$  and the intermediate loss  $\mathcal{L}_{Int}$ . The weight parameter  $\alpha$  is set to 1.0.

1) *Image reconstruction loss*: To achieve high-quality reconstruction of the degraded image, the  $\ell_2$  loss function is employed to measure the difference between the restored image  $g_0$  and the HR ground-truth  $u_{HR}^{gt}$ . It is represented as:

$$\mathcal{L}_{Rec} = \|g_0 - u_{HR}^{gt}\|_2. \quad (13)$$

2) *Intermediate loss*: In deep-supervising learning, intermediate loss assists in training by offering additional guidance in various stage modules. This loss can improve feature representation, accelerate convergence, and improve the model's predictive abilities. To verify that each module is executing its designated function, we incorporated an intermediate loss defined as follows:

$$\mathcal{L}_{Int} = \sum_{i \in \mathcal{A}} \|g_i - u_i^{gt}\|_2, \quad (14)$$

where  $\mathcal{A}$  represents the subscripts for the intermediate predictions of HDI-PRNet. In particular, the intermediate loss regulates distinct modules responsible for specific learning

TABLE I  
ABLATION STUDY OF MODEL DEGRADATION ORDERS.

Network type	1st-order degradation images		2nd-order degradation images		3rd-order degradation images		Params (M)	FLOPs (G)
	PSNR (dB)	SSIM	PSNR (dB)	SSIM	PSNR (dB)	SSIM		
1st-order network	<b>31.80</b>	<b>0.8492</b>	28.81	0.7438	27.20	0.6776	8.19	167.37
2nd-order network	31.70	0.8467	<b>30.03</b>	<b>0.7931</b>	28.49	0.7350	16.39	338.72
3rd-order network	31.48	0.8428	29.95	0.7913	<b>28.64</b>	<b>0.7408</b>	24.58	515.43

activities, each with a clear objective, which significantly enhances the interpretability of the proposed network.

#### IV. NUMERICAL EXPERIMENTS

##### A. Implementation Details

1) **Datasets:** In our experimental investigation of different restoration methods for remote sensing, we have chosen to focus on well-known datasets, namely AID [40], WHU-RS19 [41], and WHU Building [42].

- 1) **AID dataset** [40] consists of 10,000 images, each measuring  $600 \times 600$  pixels with a spatial resolution of 0.5 m/pixel (0.5 meters per pixel). This collection represents 30 different land-use categories, such as airports, farmlands, beaches, deserts, etc.
- 2) **WHU-RS19 dataset** [41] consists of 1005 remote sensing images, each  $600 \times 600$  pixels in size, with a maximum spatial resolution of 0.5 m/pixel. The dataset represents 19 unique land types, such as airports, bridges, mountains, and rivers, among others.
- 3) **WHU Building dataset** [42] features more than 220,000 individual buildings derived from aerial imagery at a spatial resolution of 0.075 m in Christchurch, New Zealand. The WHU Building dataset contains 4736 and 1036 aerial images with  $512 \times 512$  resolution for the training and validation sets.

For training and assessment of our methodology, the AID and WHU Building sets are used for training, while WHU-RS19 serves as a test set.

2) **High-order Degradation Simulation:** Inspired by the image degradation mechanism as detailed in [29], we employ a high-order degradation model to simulate real degradation on hyper-resolution datasets. Initially, the blurring model is used on the original image, followed by applying the undersampling operator to the blurred image. Lastly, the noise model is applied to the image that has been both undersampled and blurred. We continuously implement these degradation models to simulate the  $k$ -order hybrid image degradation (see Fig. 1(a) for more details).

To simulate the  $\ell$ -th blur degradation  $\mathcal{B}_\ell(\cdot)$ , we configure the blur kernel size as  $2n + 1$  where  $n$  is randomly selected from the set  $\{3, 4, \dots, 10\}$ . We employ the selection strategy to determine the blur kernel type: 1) the sinc filter is chosen with a probability of 0.1 to simulate the ringing and overshoot effects in images; 2) the isotropic Gaussian, anisotropic Gaussian, isotropic generalized Gaussian, anisotropic generalized Gaussian and isotropic / anisotropic plateau-shaped blur

kernels are generated with a probability of 0.9, following proportions of 0.45:0.25:0.12:0.03:0.12:0.03. The Gaussian blur standard deviation is selected between 0.1 and 2.0, but for the second degradation stage, this range is narrowed to 0.1 to 1.0. The shape parameters for the generalized Gaussian and plateau-shaped kernels are chosen from 0.5 to 4 and 1 to 2, respectively. The second stage of blur degradation is omitted with a probability of 0.2.

To simulate the  $\ell$ -th resizing degradation  $\mathcal{S}_\ell(\cdot)$ , we perform upsampling, downsampling, or maintain the original image resolution with probabilities of 0.2, 0.7, and 0.1, respectively (reconfigured to probabilities of 0.3, 0.4, and 0.3 during the second degradation stage). The resizing scale is randomly chosen between 0.5 and 1.5 (ranging between 0.8 and 1.2 for the second degradation step). The sampling method is randomly selected from bilinear interpolation, bicubic interpolation, and area resizing. Finally, we resize the images to achieve the desired low-resolution.

To simulate the degradation of noise pollution  $\mathcal{N}_\ell(\cdot)$  at  $\ell$ -th stage, Gaussian and Poisson noise are incorporated, each with a probability of 0.5. The level of Gaussian noise ranged from 1 to 25, and the level of Poisson noise from 0.05 to 2.5. In contrast, the noise level used in the second degradation stage ranges from 1 to 20 for Gaussian and 0.05 to 2.0 for Poisson. Furthermore, gray noise was applied with a probability of 0.4.

3) **Evaluation Metrics:** We evaluate the image restoration in remote sensing using peak signal-to-noise ratio (PSNR), structural similarity (SSIM) [43], and the blind/referenceless image spatial quality evaluator (BRISQUE) [44]. The superior restoration performance is reflected in elevated PSNR and SSIM values, along with reduced BRISQUE values.

4) **Compared Methods:** We conduct a group of studies with fourteen other methods to evaluate the performance of the proposed method. We compare our MVMS-RCN with general image restoration approaches such as RCAN [10], SwinIR [12], RDN [17], SAN [20], DAT [22], D-DBPN [45], CAT [46], and RGT [47], as well as super-resolution methods in remote sensing, such as MHAN [24], TTST [26], HAUNet [27], TransENet [28], CTNet [48], and HSENet [49].

5) **Training Settings:** We use a batch size of 32 to train our model. Each input of the LR image is randomly cropped to dimensions of  $64 \times 64$ , with a total of 200K training iterations. The training patches undergo augmentation via random horizontal flips and rotations. To keep fair comparisons, we use the Adam optimizer with parameters  $\beta_1 = 0.9$  and  $\beta_2 = 0.99$ . The initial learning rate is set as  $2 \times 10^{-4}$ , which is halved at all milestones of [20K, 120K, 160K, 180K]. Our models are



Fig. 3. Visualization comparison for super-resolution scales x2, x3 and x4 on WHU-RS19 dataset.

TABLE II  
COMPARISON FOR DIFFERENT LOSS WEIGHT PARAMETERS  $\alpha$  ON AIRS DATASET.

Loss weight $\alpha$	PSNR (dB)	SSIM
0	29.96	0.7915
0.1	30.06	0.7933
0.5	30.04	0.7934
1.0	30.03	0.7931

implemented using PyTorch and run on a Nvidia A100 GPU.

### B. Ablation Study

We conduct extensive ablation studies to evaluate the contributions of each component within the proposed HDI-PRNet framework. These experiments involve analyzing the advantages of high-order networks, the loss weight, the denoise

TABLE III  
ABLATION STUDY OF THE DENOISING MODULE CONFIGURATION.

Scale number		Block number		Params (M)	FLOPs (G)	PSNR (dB)	SSIM
1	2	1	2				
✓			✓	7.75	279.94	29.93	0.7893
	✓		✓	10.04	295.19	29.97	0.7904
		✓	✓	11.98	298.64	29.98	0.7923
		✓	✓	16.39	338.72	30.03	0.7931

module architecture, the number of Neumann series expansion orders, and the effectiveness of DDLB.

1) *Evaluation for high-order degradation*: To demonstrate the advantages of high-order framework, we perform ablation studies, as shown in Table I. Our analysis assesses the perfor-



TABLE IV  
ABLATION STUDY FOR DIFFERENT ORDERS OF THE NEUMANN SERIES  
EXPANSION IN DEBLURRING MODULE.

Orders number			Params (M)	FLOPs (G)	PSNR (dB)	SSIM
1	3	5				
✓			13.37	208.55	29.83	0.7902
	✓		14.88	273.64	29.95	0.7926
		✓	16.39	338.72	30.03	0.7931

TABLE V  
ABLATION STUDY OF DUAL-DOMAIN DEGRADATION LEARNING BLOCK.

SB	FB	DEA	Params (M)	FLOPs (G)	PSNR (dB)	SSIM
✓						
	✓		13.77	205.76	29.90	0.7892
✓	✓		16.36	338.47	30.00	0.7933
✓	✓	✓	16.39	338.72	30.03	0.7931

mance of framework with differing degradation orders across various degraded images to demonstrate their robustness. We can see from Table I that the low-order degradation network exhibits significantly decreasing performance when faced with complex high-order degraded images. In contrast, high-order degradation network achieves more consistent and superior results in different degradation images, underscoring their increased robustness. For optimal configuration, we chose the second-order degradation architecture because it provides a suitable balance between network complexity and reconstruction performance.

2) *Sensitivity of the loss weight  $\alpha$* : The WHU-RS19 dataset is used to explore the optimal value for the loss weight  $\alpha$ . As shown in Table II, setting the weight  $\alpha = 0$  results in inferior image reconstruction performance compared to the methods where  $\alpha \neq 0$ . This indicates that the intermediate loss that supervises each submodule is advantageous.

Fig. 2 illustrates the intermediate predictions and the final restored results with different loss weights. Evidently, when the weight  $\alpha$  is set to 0, each sub-module predicts an approximate black-box image, obscuring the understanding of the individual roles and impacts of each sub-module. On the other hand, incorporating the intermediate loss illustrates that the sub-modules are beneficial to their designated sub-tasks. In conclusion, to preserve the clarity of the functions of each module and to enable efficient supervised learning, we have chosen  $\alpha = 1.0$  as the loss weight.

3) *Denoising module architecture*: Table III presents an ablation study that demonstrates the impact of the architecture of the denoising module. We evaluate different denoising module configurations with diverse scales and blocks to determine their efficiency. According to Table III, the variant that employs a multi-scale architecture consistently outperforms the single-scale architecture in terms of PSNR and SSIM metrics. In addition, increasing the number of blocks also improves denoising performance. By evaluating factors such as

parameters and indices, our HDI-PRNet is designed with three scales and two blocks to implement the denoising module. Compared with the baseline model with a single scale and a single block, we see a PSNR improvement of 0.1 dB.

4) *Deblurring module architecture*: We continue our exploration by analyzing how different orders of the Neumann series expansion, specifically at orders 1, 3, and 5, influence the reconstruction performance. Table IV illustrates an improvement in performance with more expansion terms, which confirms the effectiveness of the expansion architecture. Therefore, we choose an expansion of order 5 in the deblurring module for the optimal configuration.

5) *DDL B architecture*: We evaluate the performance of DDLB by carrying out comparative analyses with several alternative variants. Table V displays the PSNR and SSIM metrics with a super-resolution scaling factor of  $\times 2$ . It is observed that focusing solely on either the spatial or frequency branch presents difficulties in efficiently recovering the image from blur degradation. The DEA module integrates these two branches more effectively than a straightforward addition. Compared to the baseline module in the spatial branch, the PSNR achieves an improvement of 0.2dB.

### C. Comparisons with other methods on WHU-RS19 dataset

In this section, we assess the effectiveness of our proposed method by comparing it with popular image restoration methods using the WHU-RS19 dataset. Tables VI, VII, and VIII present the quantitative analysis of various evaluation metrics on different super-resolution scales. Our proposed HDI-PRNet achieves the best reconstruction performance in terms of average reconstruction metrics, showing average improvements of 0.35dB, 0.24dB, and 0.08dB. Furthermore, it also produces optimal or suboptimal reconstruction results in most land-use categories.

Fig. 3 shows a visualization comparison of the restoration results obtained by different methods in the WHU-RS19 dataset. Our method significantly alleviates the degradation caused by noise, blur, and downsampling, resulting in sharper images that are visually close to the ground truth. Although other methods have attained some success, they cannot fully restore the details of texture and structure. Specifically, the restoration results of CTNet and HSENet have many artifacts. Approaches such as DAT and HAUNet have complex designed architectures that can extract richer features, but they all produce over-smoothing results. In contrast, our method not only removes noise but also effectively restores image details and edges, obtaining the clearest and most accurate remote sensing images.

Fig. 4 displays a violin-plot that serves as a tool for assessing the stability in performance of the high-order restoration framework. The plot includes three primary lines: the first quartile (Q1), the median, and the third quartile (Q3), which are useful for assessing the result's dispersion. The Q1, median and Q3 values of the proposed method are the highest, indicating better overall performance compared to other approaches. The curve in the violin-plot represents a kernel density map, reflecting the data distribution shape. As

TABLE VI

COMPARISON OF DIFFERENT SRX2 MODELS ON VARIOUS SCENE CLASSES OF WHU-RS19 (PSNR (dB)/SSIM). THE BEST AND SECOND-BEST RESULTS ARE HIGHLIGHTED IN BOLD FONT AND UNDERLINED ONES, RESPECTIVELY.

WHU-RS19	Airport	Beach	Bridge	Commercial	Desert	Farmland	FootballField	Forest	Industrial	Meadow
Methods	PSNR/SSIM	PSNR/SSIM	PSNR/SSIM	PSNR/SSIM	PSNR/SSIM	PSNR/SSIM	PSNR/SSIM	PSNR/SSIM	PSNR/SSIM	PSNR/SSIM
CTNet [48]	27.08/0.737	34.41/0.944	31.79/0.854	24.31/0.693	36.79/0.898	33.52/0.824	28.05/0.793	27.03/0.586	25.54/0.718	34.81/0.815
HSENet [49]	27.55/0.745	34.41/0.950	32.25/0.858	24.60/0.694	36.83/0.901	33.95/0.828	28.39/0.799	27.18/0.594	25.94/0.723	34.84/0.813
D-DBPN [45]	27.80/0.758	35.67/0.945	32.54/0.863	24.74/0.704	37.03/0.900	33.82/0.828	28.76/0.809	27.39/0.607	26.12/0.734	34.95/0.815
RDN [17]	27.90/0.761	36.18/0.948	32.65/0.867	24.79/0.706	37.29/0.903	34.16/0.835	28.89/0.818	27.44/0.612	26.22/0.739	35.06/0.817
TransENet [28]	27.92/0.762	36.28/0.946	32.54/0.867	24.84/0.708	37.33/0.903	33.99/0.832	29.09/0.820	27.47/0.617	26.37/0.745	34.96/0.814
RCAN [10]	27.97/0.765	36.73/0.949	32.83/0.870	24.94/0.714	37.43/0.904	34.28/0.838	29.14/0.823	27.41/0.612	26.41/0.747	35.15/0.820
SAN [20]	27.98/0.761	36.64/0.943	32.49/0.861	24.87/0.709	37.22/0.903	34.27/0.835	28.97/0.817	27.45/0.612	26.29/0.740	35.12/0.819
MHAN [24]	27.91/0.762	36.49/0.951	32.58/0.865	24.88/0.711	37.38/0.904	34.23/0.835	28.96/0.820	27.43/0.613	26.37/0.743	35.02/0.816
SwinIR [12]	27.96/0.764	37.18/0.950	32.62/0.868	24.88/0.712	37.44/0.904	34.24/0.836	29.00/0.823	27.36/0.612	26.33/0.747	35.13/0.819
HAUNet [27]	28.05/0.762	36.60/0.948	32.81/0.870	24.97/0.711	37.50/0.904	34.40/0.838	29.24/0.823	27.50/0.619	26.53/0.747	35.17/0.820
TTST [26]	27.97/0.763	36.59/0.944	32.72/0.869	24.93/0.712	37.52/0.905	34.26/0.835	29.05/0.821	27.39/0.611	26.38/0.746	35.11/0.819
CAT [46]	28.10/0.768	37.15/0.954	32.93/0.871	25.11/0.720	37.53/0.905	34.36/0.838	29.42/0.832	27.57/0.626	26.56/0.755	35.15/0.819
RGT [47]	28.19/0.771	37.18/0.949	32.83/0.872	25.09/0.719	37.63/0.906	34.50/0.841	29.37/0.831	27.50/0.624	26.56/0.754	35.21/0.821
DAT [22]	28.25/0.772	36.99/0.948	32.83/0.873	25.11/0.721	37.63/0.906	34.53/0.841	29.48/0.832	27.52/0.624	26.60/0.756	35.20/0.821
HDI-PRNet	<b>28.55/0.780</b>	<b>37.80/0.950</b>	<b>33.48/0.878</b>	<b>25.44/0.731</b>	<b>37.58/0.906</b>	<b>34.59/0.845</b>	<b>29.73/0.836</b>	<b>27.84/0.634</b>	<b>27.08/0.767</b>	<b>35.22/0.822</b>

WHU-RS19	Mountain	Park	Parking	Pond	Port	RailwayStation	Residential	River	Viaduct	Average
Methods	PSNR/SSIM	PSNR/SSIM	PSNR/SSIM	PSNR/SSIM	PSNR/SSIM	PSNR/SSIM	PSNR/SSIM	PSNR/SSIM	PSNR/SSIM	PSNR/SSIM
CTNet [48]	24.46/0.579	27.44/0.701	25.81/0.805	35.10/0.902	26.62/0.806	24.56/0.621	24.20/0.724	27.63/0.699	25.17/0.693	28.64/0.757
HSENet [49]	24.66/0.582	27.84/0.704	26.52/0.817	35.57/0.905	27.03/0.811	24.81/0.623	24.48/0.730	27.77/0.703	25.45/0.701	28.94/0.762
D-DBPN [45]	24.81/0.592	27.91/0.708	26.92/0.830	35.56/0.901	27.31/0.821	25.12/0.644	24.74/0.742	27.94/0.710	25.96/0.725	29.20/0.770
RDN [17]	24.83/0.594	27.99/0.711	26.93/0.833	35.82/0.907	27.31/0.824	25.19/0.653	24.74/0.745	28.01/0.714	26.04/0.732	29.33/0.774
TransENet [28]	24.87/0.604	28.03/0.713	26.94/0.836	35.65/0.907	27.33/0.825	25.08/0.646	24.82/0.748	27.98/0.719	26.09/0.733	29.33/0.776
RCAN [10]	24.92/0.602	28.09/0.716	27.01/0.838	35.97/0.909	27.39/0.827	25.21/0.658	24.90/0.752	28.02/0.719	26.24/0.740	29.46/0.779
SAN [20]	24.87/0.599	28.05/0.712	26.92/0.833	35.82/0.907	27.35/0.825	25.17/0.650	24.83/0.747	28.09/0.716	26.03/0.729	29.38/0.774
MHAN [24]	24.89/0.600	28.07/0.713	27.14/0.837	35.81/0.906	27.48/0.828	25.19/0.650	24.89/0.750	28.10/0.718	26.13/0.733	29.40/0.776
SwinIR [12]	24.88/0.604	28.05/0.716	26.94/0.839	35.91/0.907	27.38/0.829	25.01/0.652	24.87/0.751	27.94/0.718	26.13/0.738	29.42/0.778
HAUNet [27]	25.00/0.607	28.10/0.715	27.31/0.844	36.03/0.910	27.43/0.828	25.29/0.656	24.90/0.751	28.09/0.720	26.25/0.736	29.52/0.779
TTST [26]	24.86/0.600	28.07/0.714	27.13/0.840	35.91/0.909	27.43/0.829	25.31/0.651	24.92/0.752	28.07/0.719	26.09/0.733	29.44/0.777
CAT [46]	24.95/0.608	28.18/0.721	27.46/0.850	35.99/0.909	27.70/0.834	25.38/0.661	25.10/0.761	28.18/0.725	26.46/0.746	29.63/0.784
RGT [47]	24.95/0.610	28.25/0.722	27.27/0.845	36.02/0.910	27.67/0.834	25.31/0.662	25.10/0.761	28.15/0.725	26.46/0.749	29.63/0.784
DAT [22]	25.08/0.615	28.25/0.722	27.39/0.847	36.16/0.911	27.76/0.836	25.50/0.668	25.16/0.763	28.22/0.728	26.53/0.752	29.68/0.785
HDI-PRNet	<b>25.27/0.627</b>	<b>28.48/0.727</b>	<b>28.18/0.860</b>	<b>36.24/0.911</b>	<b>28.35/0.845</b>	<b>26.05/0.693</b>	<b>25.58/0.772</b>	<b>28.54/0.735</b>	<b>26.87/0.761</b>	<b>30.03/0.793</b>

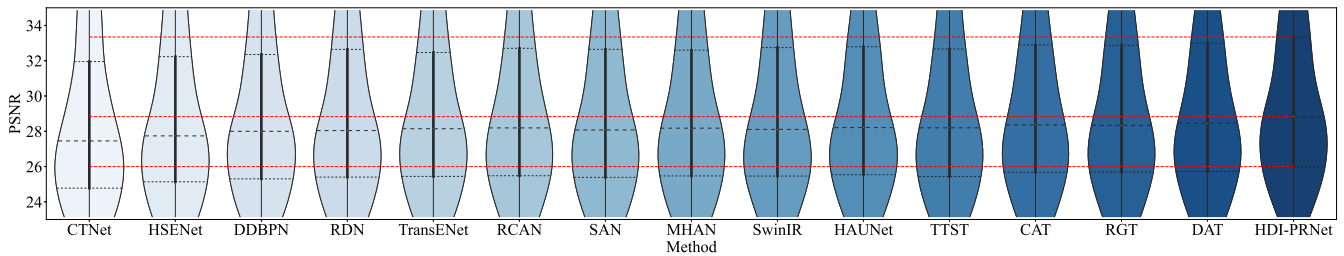


Fig. 4. PSNR violin-plot of different x2 SR methods on WHU-RS19 dataset.

depicted in Fig. 4, our method exhibits a more concentrated data distribution with less variance, contributing to greater model stability than alternative methods.

D. Comparisons on real remote sensing images

To validate the generalizability of the proposed method, we perform experiments using real remote sensing images captured by the Jilin-1, Gaofen-1, Gaofen-2, Gaofen-6, and Gaofen-7 satellites. To facilitate testing, the dataset includes 824 Jilin-1 images that have been resized to 64 × 64 pixels,

along with 400 images from each Gaofen satellite resized to 128 × 128 pixels.

The visualization comparison is shown in Fig.5. MHAN, SwinIR, DAT, and TTST have evidently enhanced image quality to a certain extent; however, they have excessively smoothed the original image, unintentionally removing some details by mistaking them for noise or artifacts. In comparison to other methods, the reconstructed image using the proposed method is significantly clearer, particularly in detail and texture, restoring these aspects more accurately and closely to the original image without producing artifacts or over-smoothing.



Fig. 5. Visualization comparison of different methods on the real satellite images.

TABLE VII

COMPARISON OF DIFFERENT SRX3 MODELS ON VARIOUS SCENE CLASSES OF WHU-RS19 (PSNR (dB)/SSIM). THE BEST AND SECOND-BEST RESULTS ARE HIGHLIGHTED IN BOLD FONT AND UNDERLINED ONES, RESPECTIVELY.

WHU-RS19	Airport	Beach	Bridge	Commercial	Desert	Farmland	FootballField	Forest	Industrial	Meadow
Methods	PSNR/SSIM	PSNR/SSIM	PSNR/SSIM	PSNR/SSIM	PSNR/SSIM	PSNR/SSIM	PSNR/SSIM	PSNR/SSIM	PSNR/SSIM	PSNR/SSIM
CTNet [48]	26.10/0.716	34.47/0.945	29.89/0.843	23.08/0.636	36.60/0.895	32.52/0.800	26.78/0.757	26.64/0.556	24.47/0.665	34.10/0.802
HSENet [49]	26.59/0.726	35.66/0.942	30.47/0.851	23.36/0.645	36.78/0.896	33.00/0.808	27.22/0.769	26.75/0.562	24.89/0.679	34.18/0.803
D-DBPN [45]	26.82/0.739	35.57/0.948	31.01/0.860	23.96/0.673	36.76/0.894	32.92/0.809	27.77/0.785	26.95/0.580	25.44/0.702	34.40/0.807
RDN [17]	26.90/0.741	36.40/0.951	31.07/0.861	23.89/0.671	37.01/0.899	33.26/0.813	27.73/0.790	26.93/0.578	25.39/0.701	34.42/0.807
TransENet [28]	27.09/0.744	36.91/0.953	31.06/0.864	23.94/0.674	36.86/0.899	33.18/0.813	27.79/0.790	27.01/0.587	25.49/0.704	34.34/0.806
RCAN [10]	27.09/0.748	36.57/0.948	31.18/0.865	23.99/0.680	37.03/0.899	33.29/0.814	27.87/0.794	27.07/0.593	25.49/0.707	34.53/0.810
SAN [20]	26.86/0.741	35.83/0.944	30.90/0.861	23.88/0.671	36.95/0.898	33.20/0.812	27.68/0.785	26.91/0.578	25.41/0.701	34.44/0.807
MHAN [24]	27.01/0.745	36.20/0.951	31.18/0.864	23.99/0.676	36.99/0.898	33.26/0.814	27.84/0.791	26.99/0.585	25.53/0.706	34.46/0.809
SwinIR [12]	27.10/0.749	37.11/0.954	31.21/0.866	24.00/0.680	37.08/0.900	33.30/0.814	27.81/0.795	27.06/0.592	25.53/0.709	34.48/0.809
HAUNet [27]	27.09/0.745	36.61/0.955	31.21/0.864	23.98/0.673	37.02/0.899	33.38/0.815	27.88/0.788	27.09/0.588	25.56/0.704	34.46/0.807
TTST [26]	27.00/0.743	35.63/0.955	31.13/0.862	23.92/0.671	36.69/0.898	33.31/0.814	27.85/0.787	27.00/0.582	25.47/0.701	34.46/0.808
CAT [46]	27.35/0.755	36.94/0.949	31.37/0.868	24.16/0.687	37.13/0.900	33.45/0.818	28.16/0.802	27.13/0.595	25.69/0.715	34.58/0.810
RGT [47]	27.31/0.755	37.29/0.955	31.37/0.869	24.16/0.687	37.14/0.900	33.47/0.819	28.19/0.804	27.13/0.596	25.69/0.716	34.54/0.809
DAT [22]	27.34/0.756	37.07/0.953	31.53/0.870	24.20/0.689	<b>37.15/0.900</b>	33.51/0.820	28.26/0.804	27.14/0.598	25.75/0.718	34.56/0.810
HDI-PRNet	<b>27.53/0.759</b>	<b>37.62/0.957</b>	<b>32.02/0.874</b>	<b>24.41/0.692</b>	36.97/0.900	<b>33.66/0.822</b>	<b>28.61/0.808</b>	<b>27.23/0.596</b>	<b>26.02/0.723</b>	<b>34.60/0.811</b>

WHU-RS19	Mountain	Park	Parking	Pond	Port	RailwayStation	Residential	River	Viaduct	Average
Methods	PSNR/SSIM	PSNR/SSIM	PSNR/SSIM	PSNR/SSIM	PSNR/SSIM	PSNR/SSIM	PSNR/SSIM	PSNR/SSIM	PSNR/SSIM	PSNR/SSIM
CTNet [48]	23.53/0.501	26.72/0.653	24.04/0.735	32.81/0.883	25.21/0.785	23.87/0.575	22.79/0.660	26.57/0.648	24.22/0.638	27.59/0.720
HSENet [49]	23.74/0.514	27.05/0.661	24.59/0.749	33.12/0.888	25.48/0.792	24.31/0.596	23.17/0.673	26.93/0.658	24.59/0.653	27.98/0.729
D-DBPN [45]	23.93/0.525	27.31/0.672	25.27/0.775	33.36/0.890	26.06/0.805	24.78/0.623	23.57/0.693	27.14/0.668	25.10/0.682	28.31/0.743
RDN [17]	23.95/0.533	27.35/0.673	25.19/0.776	33.46/0.893	25.97/0.806	24.80/0.626	23.46/0.692	27.19/0.669	25.08/0.684	28.38/0.745
TransENet [28]	23.97/0.540	27.38/0.675	25.54/0.788	33.32/0.893	25.98/0.808	24.91/0.628	23.63/0.700	27.23/0.675	25.09/0.686	28.44/0.748
RCAN [10]	24.03/0.544	27.46/0.679	25.17/0.784	33.55/0.895	26.03/0.812	24.96/0.640	23.51/0.699	27.30/0.678	25.28/0.696	28.48/0.751
SAN [20]	23.91/0.530	27.35/0.673	25.12/0.774	33.41/0.892	25.89/0.805	24.73/0.623	23.50/0.694	27.14/0.668	25.03/0.679	28.31/0.743
MHAN [24]	24.00/0.538	27.43/0.676	25.23/0.782	33.57/0.894	26.09/0.810	24.94/0.634	23.58/0.698	27.25/0.673	25.21/0.688	28.45/0.748
SwinIR [12]	24.05/0.547	27.44/0.679	25.44/0.790	33.55/0.895	26.14/0.814	24.97/0.637	23.61/0.703	27.29/0.677	25.26/0.696	28.53/0.752
HAUNet [27]	24.04/0.539	27.35/0.671	25.64/0.792	33.54/0.893	26.07/0.808	24.93/0.627	23.65/0.700	27.33/0.675	25.16/0.685	28.51/0.748
TTST [26]	23.98/0.535	27.40/0.674	25.39/0.779	33.41/0.892	26.04/0.807	24.77/0.621	23.60/0.698	27.26/0.674	25.17/0.686	28.38/0.746
CAT [46]	<b>24.13/0.553</b>	27.47/0.681	25.80/0.804	33.59/0.896	26.33/0.818	25.18/0.647	23.77/0.710	27.38/0.683	25.47/0.707	28.67/0.757
RGT [47]	24.09/0.550	<u>27.57/0.683</u>	25.66/0.799	<u>33.73/0.897</u>	<u>26.34/0.819</u>	<u>25.25/0.652</u>	23.77/0.710	<u>27.41/0.684</u>	25.47/0.708	28.70/0.758
DAT [22]	<u>24.12/0.552</u>	27.53/0.682	<u>25.89/0.803</u>	<u>33.71/0.897</u>	<u>26.37/0.819</u>	25.18/0.651	<u>23.79/0.712</u>	<u>27.44/0.684</u>	<u>25.52/0.709</u>	<u>28.72/0.759</u>
HDI-PRNet	<b>24.24/0.550</b>	<b>27.65/0.684</b>	<b>26.59/0.818</b>	<u>33.74/0.896</u>	<b>26.82/0.825</b>	<b>25.55/0.662</b>	<b>24.31/0.722</b>	<b>27.53/0.685</b>	<b>25.66/0.711</b>	<b>28.96/0.762</b>

Furthermore, we train the MHAN and SwinIR models employing bicubic degradation and evaluate them on real remote sensing datasets. Both MHAN (bicubic) and SwinIR (bicubic) demonstrate a slight but not evident improvement in the quality of real remote sensing images, which further demonstrates the rationality of our model's architecture and configurations.

Since real remote sensing images lack HR ground truth, we employ BRISQUE to evaluate the predicted results. As shown in Table IX, HDI-PRNet achieves the best or second-best results on real images from five different satellites. Although MHAN records the highest score on Jilin-1, its predictions are visually over-smoothed, which is not preferable. Overall, these significant improvements in both visual quality and reconstruction performance metrics strongly show the effectiveness and practical utility of HDI-PRNet to restore real remote sensing images, further highlighting the excellence of our proposed HDI-PRNet.

## V. CONCLUSION

In this paper, we proposed a novel remote sensing high-order restoration framework. Our framework is based on

the inverse design of the high-order degradation model to gradually restore the image, which provides a theoretical basis for the design of the DL framework. In addition, we introduced a denoising module that simulates the proximal mapping operator to learn the denoising prior representation of the current image. To solve the deblurring problem, we proposed a deblurring module that ensures the accurate representation of the degradation operator based on the expansion of the Neumann series and dual-domain degradation learning. We also introduced an intermediate loss in the middle of the network so that each module has supervision and the overall network is more interpretable. We performed several high-order degradation reconstruction experiments on WHU-RS19 and real remote sensing images. Experimental results show that our HDI-PRNet achieves competitive results on both synthetic and real images.

In the future, we believe that our method can be extended to other image restoration problems to perform more complex and diverse image restoration tasks, such as image dehazing and image artifact removal, and obtain better restoration performance on real images.

TABLE VIII

COMPARISON OF DIFFERENT SRX4 MODELS ON VARIOUS SCENE CLASSES OF WHU-RS19 (PSNR (dB)/SSIM). THE BEST AND SECOND-BEST RESULTS ARE HIGHLIGHTED IN BOLD FONT AND UNDERLINED ONES, RESPECTIVELY.

WHU-RS19	Airport	Beach	Bridge	Commercial	Desert	Farmland	FootballField	Forest	Industrial	Meadow
Methods	PSNR/SSIM	PSNR/SSIM	PSNR/SSIM	PSNR/SSIM	PSNR/SSIM	PSNR/SSIM	PSNR/SSIM	PSNR/SSIM	PSNR/SSIM	PSNR/SSIM
CTNet [48]	24.88/0.655	35.59/0.938	30.01/0.835	22.09/0.552	35.71/0.892	32.09/0.790	25.39/0.701	25.56/0.470	23.62/0.605	33.58/0.797
HSENet [49]	25.64/0.695	37.12/0.947	30.86/0.851	22.67/0.598	<u>36.25/0.897</u>	32.75/0.804	26.28/0.738	26.02/0.511	24.48/0.657	33.92/0.800
D-DBPN [45]	25.59/0.694	36.30/0.942	30.92/0.851	22.72/0.599	36.06/0.895	32.62/0.802	26.24/0.737	25.97/0.506	24.46/0.655	33.86/0.800
RDN [17]	25.52/0.693	36.85/0.945	30.85/0.852	22.62/0.595	<u>36.21/0.897</u>	32.72/0.803	26.15/0.738	25.93/0.509	24.36/0.652	33.89/0.800
TransENet [28]	25.69/0.696	37.40/0.948	30.88/0.854	22.73/0.600	<u>36.03/0.897</u>	32.74/0.804	26.39/0.745	26.08/0.517	24.54/0.659	33.92/0.801
RCAN [10]	25.68/0.702	37.07/0.946	30.93/0.855	22.76/0.606	<u>36.20/0.897</u>	32.86/0.806	26.35/0.746	26.06/0.516	24.61/0.665	33.90/0.800
SAN [20]	25.53/0.692	36.65/0.944	30.81/0.850	22.61/0.593	36.19/0.896	32.69/0.802	26.11/0.733	25.94/0.506	24.40/0.651	33.90/0.799
MHAN [24]	25.64/0.696	37.20/0.947	30.69/0.851	22.70/0.598	<u>36.24/0.897</u>	32.75/0.803	26.27/0.740	25.98/0.512	24.49/0.656	33.93/0.800
SwinIR [12]	25.79/0.704	37.49/0.949	30.99/0.855	22.81/0.609	36.31/0.898	32.90/0.807	26.47/0.750	26.12/0.521	24.66/0.668	33.96/0.801
HAUNet [27]	25.67/0.695	37.16/0.947	30.87/0.852	22.71/0.598	<u>36.17/0.897</u>	32.89/0.806	26.42/0.742	26.11/0.518	24.55/0.658	33.95/0.800
TTST [26]	25.76/0.703	37.21/0.948	30.85/0.854	22.80/0.607	<u>36.23/0.898</u>	32.89/0.806	26.46/0.748	26.09/0.519	24.68/0.667	33.93/0.801
CAT [46]	25.84/0.706	37.15/0.947	31.01/0.855	22.85/0.611	<u>36.33/0.898</u>	33.00/0.809	26.62/0.755	26.11/0.521	24.78/0.673	<u>34.04/0.802</u>
RGT [47]	<u>25.93/0.710</u>	<b>37.60/0.949</b>	31.25/0.858	22.91/0.613	<u>36.37/0.898</u>	<u>33.05/0.810</u>	<u>26.72/0.758</u>	26.15/0.523	24.85/0.675	<u>34.06/0.802</u>
DAT [22]	<u>25.92/0.710</u>	<u>37.54/0.949</u>	<u>31.28/0.858</u>	<u>22.92/0.614</u>	<b>36.41/0.898</b>	<u>33.05/0.810</u>	<b>26.71/0.758</b>	<u>26.16/0.522</u>	<u>24.87/0.676</u>	<u>34.06/0.802</u>
HDI-PRNet	<b>26.10/0.712</b>	<u>36.88/0.948</u>	<b>31.61/0.862</b>	<b>23.05/0.615</b>	<u>36.40/0.898</u>	<b>33.09/0.811</b>	<u>26.87/0.757</u>	<b>26.19/0.526</b>	<u>24.94/0.674</u>	<b>34.07/0.803</b>

WHU-RS19	Mountain	Park	Parking	Pond	Port	RailwayStation	Residential	River	Viaduct	Average
Methods	PSNR/SSIM	PSNR/SSIM	PSNR/SSIM	PSNR/SSIM	PSNR/SSIM	PSNR/SSIM	PSNR/SSIM	PSNR/SSIM	PSNR/SSIM	PSNR/SSIM
CTNet [48]	23.01/0.433	25.38/0.585	23.10/0.676	30.22/0.838	24.27/0.736	23.05/0.501	21.79/0.586	25.98/0.606	23.08/0.562	26.74/0.671
HSENet [49]	23.43/0.482	25.87/0.612	24.30/0.738	30.81/0.850	25.04/0.771	23.96/0.570	22.62/0.643	26.54/0.641	24.13/0.631	27.49/0.707
D-DBPN [45]	23.37/0.474	25.81/0.612	24.29/0.738	30.72/0.848	25.14/0.771	23.92/0.569	22.64/0.640	26.48/0.637	24.20/0.635	27.42/0.705
RDN [17]	23.39/0.479	25.83/0.612	24.16/0.733	30.74/0.848	25.01/0.769	23.96/0.572	22.52/0.637	26.47/0.638	24.16/0.635	27.42/0.705
TransENet [28]	23.48/0.488	25.92/0.615	24.52/0.752	30.83/0.851	25.20/0.775	24.05/0.572	22.77/0.651	26.57/0.644	24.23/0.638	27.56/0.710
RCAN [10]	23.46/0.489	25.94/0.617	24.39/0.752	30.82/0.852	25.14/0.777	24.10/0.583	22.68/0.652	26.55/0.644	24.37/0.647	27.55/0.713
SAN [20]	23.37/0.474	25.81/0.611	24.11/0.731	30.72/0.848	24.96/0.768	23.87/0.564	22.53/0.637	26.42/0.636	24.03/0.623	27.38/0.702
MHAN [24]	23.42/0.481	25.89/0.614	24.19/0.740	30.78/0.850	25.08/0.772	23.96/0.571	22.59/0.644	26.50/0.640	24.18/0.634	27.48/0.707
SwinIR [12]	23.50/0.492	25.95/0.619	24.75/0.762	30.87/0.853	25.29/0.780	24.15/0.583	22.75/0.657	26.62/0.648	24.36/0.648	27.65/0.715
HAUNet [27]	23.46/0.482	25.87/0.612	24.71/0.760	30.80/0.851	25.17/0.774	24.04/0.569	22.74/0.652	26.59/0.645	24.22/0.633	27.56/0.709
TTST [26]	23.50/0.491	25.94/0.617	24.67/0.756	30.90/0.853	25.28/0.779	24.09/0.580	22.73/0.654	26.61/0.647	24.34/0.646	27.61/0.714
CAT [46]	23.50/0.489	25.96/0.620	24.91/0.770	30.91/0.854	25.38/0.782	24.27/0.589	22.86/0.662	26.64/0.649	24.48/0.656	27.70/0.718
RGT [47]	23.54/0.496	<u>26.06/0.622</u>	<u>25.01/0.772</u>	<u>30.99/0.854</u>	<u>25.45/0.785</u>	<u>24.33/0.594</u>	<u>22.94/0.664</u>	<u>26.70/0.651</u>	<u>24.56/0.658</u>	<u>27.79/0.720</u>
DAT [22]	<u>23.55/0.495</u>	<u>26.05/0.622</u>	<u>25.06/0.772</u>	<u>30.97/0.855</u>	25.43/0.784	<u>24.34/0.594</u>	<u>22.92/0.664</u>	<u>26.70/0.653</u>	<u>24.54/0.659</u>	<u>27.79/0.720</u>
HDI-PRNet	<b>23.62/0.498</b>	<b>26.21/0.623</b>	<b>25.29/0.778</b>	<u>31.09/0.854</u>	<b>25.58/0.783</b>	<b>24.52/0.601</b>	<b>23.21/0.668</b>	<u>26.74/0.652</u>	<b>24.60/0.657</b>	<b>27.87/0.721</b>

REFERENCES

[1] L. Wang, R. Li, C. Zhang, S. Fang, C. Duan, X. Meng, and P. M. Atkinson, "Unetformer: A unet-like transformer for efficient semantic segmentation of remote sensing urban scene imagery," *ISPRS Journal of Photogrammetry and Remote Sensing*, vol. 190, pp. 196–214, 2022.

[2] S. W. Zamir, A. Arora, S. Khan, M. Hayat, F. S. Khan, M.-H. Yang, and L. Shao, "Learning enriched features for fast image restoration and enhancement," *IEEE transactions on pattern analysis and machine intelligence*, vol. 45, no. 2, pp. 1934–1948, 2022.

[3] S.-J. Cho, S.-W. Ji, J.-P. Hong, S.-W. Jung, and S.-J. Ko, "Rethinking coarse-to-fine approach in single image deblurring," in *Proceedings of the IEEE/CVF international conference on computer vision*, 2021, pp. 4641–4650.

[4] X. Fan, Y. Yang, K. Chen, Y. Feng, and J. Zhang, "Nest-dgill: Nesterov-optimized deep geometric incremental learning for cs image reconstruction," *IEEE Transactions on Computational Imaging*, vol. 9, pp. 819–833, 2023.

[5] R. Dong, L. Mou, L. Zhang, H. Fu, and X. X. Zhu, "Real-world remote sensing image super-resolution via a practical degradation model and a kernel-aware network," *ISPRS Journal of Photogrammetry and Remote Sensing*, vol. 191, pp. 155–170, 2022.

[6] W. Zhang, X. Li, G. Shi, X. Chen, Y. Qiao, X. Zhang, X.-M. Wu, and C. Dong, "Real-world image super-resolution as multi-task learning," *Advances in Neural Information Processing Systems*, vol. 36, 2024.

[7] Y. Cui, W. Ren, X. Cao, and A. Knoll, "Revitalizing convolutional network for image restoration," *IEEE Transactions on Pattern Analysis and Machine Intelligence*, 2024.

[8] —, "Image restoration via frequency selection," *IEEE Transactions on Pattern Analysis and Machine Intelligence*, 2023.

[9] L. Chen, X. Chu, X. Zhang, and J. Sun, "Simple baselines for image restoration," in *European conference on computer vision*. Springer, 2022, pp. 17–33.

[10] Y. Zhang, K. Li, K. Li, L. Wang, B. Zhong, and Y. Fu, "Image super-resolution using very deep residual channel attention networks," in *Proceedings of the European conference on computer vision (ECCV)*, 2018, pp. 286–301.

[11] S. W. Zamir, A. Arora, S. Khan, M. Hayat, F. S. Khan, M.-H. Yang, and L. Shao, "Learning enriched features for real image restoration and enhancement," in *Computer Vision—ECCV 2020: 16th European Conference, Glasgow, UK, August 23–28, 2020, Proceedings, Part XXV 16*. Springer, 2020, pp. 492–511.

[12] J. Liang, J. Cao, G. Sun, K. Zhang, L. Van Gool, and R. Timofte, "Swinir: Image restoration using swin transformer," in *Proceedings of the IEEE/CVF international conference on computer vision*, 2021, pp. 1833–1844.

[13] Z. Ren, L. He, and J. Lu, "Context aware edge-enhanced gan for remote sensing image super-resolution," *IEEE Journal of Selected Topics in Applied Earth Observations and Remote Sensing*, vol. 17, pp. 1363–1376, 2024.

[14] Y. Quan, Z. Wu, and H. Ji, "Gaussian kernel mixture network for single image defocus deblurring," *Advances in Neural Information Processing Systems*, vol. 34, pp. 20812–20824, 2021.

[15] X. Wang, K. Yu, S. Wu, J. Gu, Y. Liu, C. Dong, Y. Qiao, and C. Change Loy, "Esrgan: Enhanced super-resolution generative adversarial networks," in *Proceedings of the European conference on computer*

TABLE IX  
COMPARISON OF DIFFERENT RESTORATION MODELS ON REAL SATELLITE IMAGES.

BRISQUE	HSENet	TransENet	MHAN	MHAN (Bicubic)	SwinIR	SwinIR (Bicubic)	TTST	HAUNet	DAT	HDI-PRNet
Jilin-1	41.3774	41.1180	<b>35.8704</b>	43.1953	37.1765	43.6537	37.3207	43.4201	36.8362	<u>36.5810</u>
Gaofen-1	40.3188	<u>39.6849</u>	40.2469	45.5903	41.4091	45.4889	40.9722	41.3830	40.7827	<b>39.6351</b>
Gaofen-2	<u>37.3217</u>	38.3410	37.9373	39.8892	39.3446	39.4106	39.2308	39.1100	38.5144	<b>35.9592</b>
Gaofen-6	<u>36.8403</u>	38.3920	38.3865	41.4711	38.9494	41.1936	38.7809	38.9542	38.4101	<b>36.7054</b>
Gaofen-7	37.7147	38.0881	37.7705	43.6968	38.6543	43.0609	38.3997	37.8802	<u>37.1173</u>	<b>37.0412</b>

vision (ECCV) workshops, 2018, pp. 0–0.

- [16] C. Dong, C. C. Loy, K. He, and X. Tang, “Image super-resolution using deep convolutional networks,” *IEEE transactions on pattern analysis and machine intelligence*, vol. 38, no. 2, pp. 295–307, 2015.
- [17] Y. Zhang, Y. Tian, Y. Kong, B. Zhong, and Y. Fu, “Residual dense network for image super-resolution,” in *Proceedings of the IEEE conference on computer vision and pattern recognition*, 2018, pp. 2472–2481.
- [18] —, “Residual dense network for image restoration,” *IEEE transactions on pattern analysis and machine intelligence*, vol. 43, no. 7, pp. 2480–2495, 2020.
- [19] S. W. Zamir, A. Arora, S. Khan, M. Hayat, F. S. Khan, and M.-H. Yang, “Restormer: Efficient transformer for high-resolution image restoration,” in *Proceedings of the IEEE/CVF conference on computer vision and pattern recognition*, 2022, pp. 5728–5739.
- [20] T. Dai, J. Cai, Y. Zhang, S.-T. Xia, and L. Zhang, “Second-order attention network for single image super-resolution,” in *Proceedings of the IEEE/CVF conference on computer vision and pattern recognition*, 2019, pp. 11 065–11 074.
- [21] Y. Mei, Y. Fan, and Y. Zhou, “Image super-resolution with non-local sparse attention,” in *Proceedings of the IEEE/CVF Conference on Computer Vision and Pattern Recognition*, 2021, pp. 3517–3526.
- [22] Z. Chen, Y. Zhang, J. Gu, L. Kong, X. Yang, and F. Yu, “Dual aggregation transformer for image super-resolution,” in *Proceedings of the IEEE/CVF international conference on computer vision*, 2023, pp. 12 312–12 321.
- [23] S. Lei, Z. Shi, and Z. Zou, “Super-resolution for remote sensing images via local–global combined network,” *IEEE Geoscience and Remote Sensing Letters*, vol. 14, no. 8, pp. 1243–1247, 2017.
- [24] D. Zhang, J. Shao, X. Li, and H. T. Shen, “Remote sensing image super-resolution via mixed high-order attention network,” *IEEE Transactions on Geoscience and Remote Sensing*, vol. 59, no. 6, pp. 5183–5196, 2020.
- [25] F. Xu, Y. Shi, P. Ebel, L. Yu, G.-S. Xia, W. Yang, and X. X. Zhu, “Glf-cr: Sar-enhanced cloud removal with global–local fusion,” *ISPRS Journal of Photogrammetry and Remote Sensing*, vol. 192, pp. 268–278, 2022.
- [26] Y. Xiao, Q. Yuan, K. Jiang, J. He, C.-W. Lin, and L. Zhang, “Ttst: A top-k token selective transformer for remote sensing image super-resolution,” *IEEE Transactions on Image Processing*, 2024.
- [27] J. Wang, B. Wang, X. Wang, Y. Zhao, and T. Long, “Hybrid attention-based u-shaped network for remote sensing image super-resolution,” *IEEE Transactions on Geoscience and Remote Sensing*, vol. 61, pp. 1–15, 2023.
- [28] S. Lei, Z. Shi, and W. Mo, “Transformer-based multistage enhancement for remote sensing image super-resolution,” *IEEE Transactions on Geoscience and Remote Sensing*, vol. 60, pp. 1–11, 2021.
- [29] X. Wang, L. Xie, C. Dong, and Y. Shan, “Real-esrgan: Training real-world blind super-resolution with pure synthetic data,” in *Proceedings of the IEEE/CVF international conference on computer vision*, 2021, pp. 1905–1914.
- [30] K. Zhang, J. Liang, L. Van Gool, and R. Timofte, “Designing a practical degradation model for deep blind image super-resolution,” in *Proceedings of the IEEE/CVF International Conference on Computer Vision*, 2021, pp. 4791–4800.
- [31] V. Potlapalli, S. W. Zamir, S. Khan, and F. Khan, “Promptir: Prompting for all-in-one image restoration,” in *Thirty-seventh Conference on Neural Information Processing Systems*, 2023.
- [32] X. Kong, C. Dong, and L. Zhang, “Towards effective multiple-in-one image restoration: A sequential and prompt learning strategy,” *arXiv preprint arXiv:2401.03379*, 2024.
- [33] J. Gu, H. Lu, W. Zuo, and C. Dong, “Blind super-resolution with iterative kernel correction,” in *Proceedings of the IEEE/CVF Conference on Computer Vision and Pattern Recognition*, 2019, pp. 1604–1613.
- [34] Y. Huang, S. Li, L. Wang, T. Tan *et al.*, “Unfolding the alternating optimization for blind super resolution,” *Advances in Neural Information Processing Systems*, vol. 33, pp. 5632–5643, 2020.
- [35] X. Fan, K. Chen, H. Yi, Y. Yang, and J. Zhang, “Mvms-rcn: A dual-domain unified ct reconstruction with multi-sparse-view and multi-scale refinement-correction,” *IEEE Transactions on Computational Imaging*, pp. 1–14, 2024.
- [36] X. Fan, Y. Yang, and J. Zhang, “Deep geometric distillation network for compressive sensing mri,” in *2021 IEEE EMBS International Conference on Biomedical and Health Informatics (BHI)*, 2021, pp. 1–4.
- [37] K. Zhang, L. V. Gool, and R. Timofte, “Deep unfolding network for image super-resolution,” in *Proceedings of the IEEE/CVF conference on computer vision and pattern recognition*, 2020, pp. 3217–3226.
- [38] Y. Quan, Z. Wu, and H. Ji, “Neumann network with recursive kernels for single image defocus deblurring,” in *Proceedings of the IEEE/CVF Conference on Computer Vision and Pattern Recognition*, 2023, pp. 5754–5763.
- [39] X. Mao, Y. Liu, F. Liu, Q. Li, W. Shen, and Y. Wang, “Intriguing findings of frequency selection for image deblurring,” in *Proceedings of the AAAI Conference on Artificial Intelligence*, vol. 37, no. 2, 2023, pp. 1905–1913.
- [40] G.-S. Xia, J. Hu, F. Hu, B. Shi, X. Bai, Y. Zhong, L. Zhang, and X. Lu, “Aid: A benchmark data set for performance evaluation of aerial scene classification,” *IEEE Transactions on Geoscience and Remote Sensing*, vol. 55, no. 7, pp. 3965–3981, 2017.
- [41] D. Dai and W. Yang, “Satellite image classification via two-layer sparse coding with biased image representation,” *IEEE Geoscience and remote sensing letters*, vol. 8, no. 1, pp. 173–176, 2010.
- [42] S. Ji, S. Wei, and M. Lu, “Fully convolutional networks for multisource building extraction from an open aerial and satellite imagery data set,” *IEEE Transactions on geoscience and remote sensing*, vol. 57, no. 1, pp. 574–586, 2018.
- [43] Z. Wang, A. C. Bovik, H. R. Sheikh, and E. P. Simoncelli, “Image quality assessment: from error visibility to structural similarity,” *IEEE transactions on image processing*, vol. 13, no. 4, pp. 600–612, 2004.
- [44] A. Mittal, A. K. Moorthy, and A. C. Bovik, “No-reference image quality assessment in the spatial domain,” *IEEE Transactions on image processing*, vol. 21, no. 12, pp. 4695–4708, 2012.
- [45] M. Haris, G. Shakhnarovich, and N. Ukita, “Deep back-projection networks for super-resolution,” in *Proceedings of the IEEE conference on computer vision and pattern recognition*, 2018, pp. 1664–1673.
- [46] Z. Chen, Y. Zhang, J. Gu, L. Kong, X. Yuan *et al.*, “Cross aggregation transformer for image restoration,” *Advances in Neural Information Processing Systems*, vol. 35, pp. 25 478–25 490, 2022.
- [47] Z. Chen, Y. Zhang, J. Gu, L. Kong, and X. Yang, “Recursive generalization transformer for image super-resolution,” in *ICLR*, 2024.
- [48] S. Wang, T. Zhou, Y. Lu, and H. Di, “Contextual transformation network for lightweight remote-sensing image super-resolution,” *IEEE Transactions on Geoscience and Remote Sensing*, vol. 60, pp. 1–13, 2021.
- [49] S. Lei and Z. Shi, “Hybrid-scale self-similarity exploitation for remote sensing image super-resolution,” *IEEE Transactions on Geoscience and Remote Sensing*, vol. 60, pp. 1–10, 2021.